

# Universal law for diffusive mass transport through mycelial networks

Stefan Schmidededer<sup>1</sup>  | Henri Müller<sup>1</sup>  | Lars Barthel<sup>2</sup>  | Tiaan Friedrich<sup>1</sup>  | Ludwig Niessen<sup>3</sup>  | Vera Meyer<sup>2</sup>  | Heiko Briesen<sup>1</sup> 

<sup>1</sup>School of Life Sciences Weihenstephan, Chair of Process Systems Engineering, Technical University of Munich, Freising, Germany

<sup>2</sup>Institute of Biotechnology, Faculty III Process Sciences, Chair of Applied and Molecular Microbiology, Technische Universität Berlin, Berlin, Germany

<sup>3</sup>School of Life Sciences Weihenstephan, Chair of Technical Microbiology, Technical University of Munich, Freising, Germany

## Correspondence

Heiko Briesen, Technical University of Munich, Chair of Process Systems Engineering, Gregor-Mendel-Str. 4, 85354 Freising, Germany.

Email: [heiko.briesen@tum.de](mailto:heiko.briesen@tum.de)

## Funding information

Deutsche Forschungsgemeinschaft, Grant/Award Numbers: 198187031, 315305620, 315384307, 427889137

## Abstract

Filamentous fungal cell factories play a pivotal role in biotechnology and circular economy. Hyphal growth and macroscopic morphology are critical for product titers; however, these are difficult to control and predict. Usually pellets, which are dense networks of branched hyphae, are formed during industrial cultivations. They are nutrient- and oxygen-depleted in their core due to limited diffusive mass transport, which compromises productivity of bioprocesses. Here, we demonstrate that a generalized law for diffusive mass transport exists for filamentous fungal pellets. Diffusion computations were conducted based on three-dimensional X-ray microtomography measurements of 66 pellets originating from four industrially exploited filamentous fungi and based on 3125 Monte Carlo simulated pellets. Our data show that the diffusion hindrance factor follows a scaling law with respect to the solid hyphal fraction. This law can be harnessed to predict diffusion of nutrients, oxygen, and secreted metabolites in any filamentous pellets and will thus advance the rational design of pellet morphologies on genetic and process levels.

## KEY WORDS

diffusive mass transport, filamentous fungal pellets, three-dimensional morphological measurements and simulations, X-ray microcomputed tomography

## 1 | INTRODUCTION

Fungal biotechnology is key for the transition from a petroleum-based economy into a bio-based circular economy. A thinktank consisting of leading European and American researchers and global business leaders concluded that this biotech sector can help to achieve 10 of the United Nations' 17 sustainable development goals (Meyer et al., 2020). Filamentous fungi are the only microorganisms that can fully degrade renewable lignocellulosic biomass and sustainably transform it into food, feed, chemicals, fuels, commodities, textiles, composite materials, antibiotics, and other drugs (Meyer et al., 2020). Their ability to perform complex posttranslational

modifications (Wang et al., 2020), their greatly expanded natural protein secretion apparatus (Ward, 2012), and the enormous potential of the secondary metabolome to produce bioactive molecules (Brakhage, 2013; Keller, 2019; Nielsen et al., 2017) make filamentous fungi a favorable host for many applications (Wösten, 2019).

Filamentous fungi are usually cultivated under submerged conditions in which their macromorphology varies from loose disperse mycelia to dense hyphal networks called pellets (Papagianni, 2004; Veiter et al., 2018). The evolution of these macromorphologies from spores, germlings, and hyphae (collectively, structures of micromorphologies) is a multifactorial process and difficult to predict. A recent review highlighted all known genetic, physiologic, medium,

and process parameters that impact the development of micro- and macromorphologies of filamentous fungi, and it also discussed all relevant advantages and disadvantages of macromorphologies with regard to the production of fungal-based bioprocesses (Cairns et al., 2019). In brief, cultivations with **disperse mycelia** allow better **homogenous distribution of nutrients and oxygen** but behave as **non-Newtonian fluids**, whereas cultivations with **pellets** behave as **Newtonian fluids** but suffer from **nutrient and oxygen limitation in the pellet cores**. For *Aspergillus niger* and *Penicillium chrysogenum* pellets, it was shown that **oxygen was often only available in the outer 200 µm** (Hille et al., 2005; Wittier et al., 1986), whereas pellet size could range from a millimeter to a centimeter in size. The areas beyond this limit are likely hypoxic and **do not sustain growth and/or product formation**.

Two factors determine the concentration of nutrients and products inside pellets (Celler et al., 2012; Cui et al., 1998; Lejeune & Baron, 1997; Meyerhoff et al., 1995): the **fungal metabolic rate** and the **transport through the filamentous network**. The transport is mainly driven by **diffusion**, which is hindered by the dense hyphal network (Hille et al., 2005). This transport limitation results in **heterogeneity and substrate limitation inside pellets** (Hille et al., 2009; Veiter et al., 2020; Wittier et al., 1986; Zacchetti et al., 2018). The following three prerequisites are necessary to compute the concentration profile of any nutrient or product within a pellet (Celler et al., 2012; Cui et al., 1998; Lejeune & Baron, 1997; Meyerhoff et al., 1995): (1) the **micro- and macromorphologies of a pellet** are known, (2) the **correlation between the morphology and the effective diffusivity** of the nutrient or product is known, and (3) the **metabolic rate**, which is also dependent on (1), can be calculated. Notably, the metabolic rate could be estimated if the first two prerequisites and the concentration profile are known. We, therefore, recently harnessed X-ray microcomputed tomography ( $\mu$ CT) and three-dimensional (3D) image analysis to determine the location and number of tips, branches, and hyphal material within whole fungal pellets to meet the first two requirements (Schmideder, Barthel, Friedrich, et al., 2019; Schmideder, Barthel, Müller, et al., 2019). Mathematically, the concentration profile of any molecule  $i$  within the voids of a pellet could be described by a **diffusion reaction equation** (Celler et al., 2012; Meyerhoff et al., 1995), where the reaction term describes the **consumption** or the **production** of the molecule. We focused on the diffusion term, where the effective diffusion coefficient  $D_{i,\text{eff}}$  of component  $i$  determines the diffusivity and can be expressed as (Becker et al., 2011):

$$D_{i,\text{eff}} = D_{i,\text{bulk}} k_{\text{eff}}(\vec{m}) \quad (1)$$

where  $\vec{m}$  is the vector for **morphological properties**, and  $k_{\text{eff}}(\vec{m})$  is the **geometrical diffusion hindrance**. The diffusion coefficient in the bulk medium  $D_{i,\text{bulk}}$  can be estimated from medium conditions (Yaws, 2009). Thus,  $k_{\text{eff}}(\vec{m})$ , which is independent of the diffusing component (Becker et al., 2011), is the only unknown variable to determine  $D_{i,\text{eff}}$ . It has to be mentioned that  $k_{\text{eff}}^{-1}$  is similar to the **formation factor**, which is often applied to describe the diffusivity, conductivity, or

permeability through porous media (Tomadakis & Robertson, 2005). In our recent study (Schmideder, Barthel, Müller, et al., 2019), we proposed the preliminary correlation  $k_{\text{eff}} = (1 - c_h)^2$  for one of the **main fungal cell factories, *A. niger***, where  $c_h$  is the **hyphal fraction** (equal to solid fraction).

In the current study, we investigated the **correlation between the effective diffusivity and the morphology** of more than 60  $\mu$ CT measured pellets from four fungal cell factories (*A. niger*, *P. chrysogenum*, *Rhizopus oryzae*, and *R. stolonifer*) and more than 3000 Monte Carlo simulated pellets. We considered the diffusion through filamentous networks with different resolutions because **image resolution can influence computed material properties** (Schmideder, Barthel, Müller, et al., 2019; Velichko et al., 2009). Based on the measurements and simulations, we propose here a generalized law for the diffusion of nutrients, oxygen, and fungal metabolites through hyphal networks. This law enables, for the first time, the **estimation of metabolic rates at any point within a pellet** and forms the mathematical foundation for future targeted genetic and process engineering strategies.

## 2 | MATERIALS AND METHODS

### 2.1 | Preparation of pellets

To obtain pellet structures of morphologically different strains of industrially relevant fungal species, we cultivated the **hyperbranching *A. niger* MF22.4 ( $\Delta racA$ )** and its parental strain MF19.5 (Fiedler et al., 2018; Kwon et al., 2011), ***P. chrysogenum* MUM17.85** (indoor paint, Micoteca da Universidade do Minho), ***R. stolonifer*** (isolated organisms), and ***R. oryzae* CBS 607.68** (unknown source). Sporangiospores (*Rhizopus* spp.) and conidiospores (*A. niger* and *P. chrysogenum*) of all strains were obtained from agar plate cultures using standard procedures for filamentous fungi (Bennet & Lasure, 1991). Erlenmeyer flasks were inoculated with the spores and cultivated for 24–48 h until pellets became visible. Pellets were carefully removed by pipetting, washed with sterile tap water, frozen while they were floating in water, and subsequently freeze dried to preserve their structure (Schmideder, Barthel, Friedrich, et al., 2019). For detailed description of pellet preparation, we refer to Supplementary Protocol 1.

### 2.2 | X-ray microcomputed tomography

To obtain the 3D fibrous network of freeze dried pellets,  $\mu$ CT measurements were performed based on the method reported previously (Schmideder, Barthel, Friedrich, et al., 2019). Pellets were fixed on top of a sample holder for image acquisition. Then, at least 2.000 **two-dimensional projections from different angles** were acquired using a  $\mu$ CT system (XCT-1600HR; Matrix Technologies) and subsequently reconstructed to 3D images with custom-designed software (Matrix Technologies) that is based on CERA (Siemens). Images

were taken with a voxel size of 1, 2, 3, and 4  $\mu\text{m}$ , respectively. For further information, we refer to Supplementary Protocol 2.

## 2.3 | Image processing

Image processing was applied on the 3D  $\mu\text{CT}$ -images of the pellets, based on the methods described previously (Schmideder, Barthel, Friedrich, et al., 2019; Schmideder, Barthel, Müller, et al., 2019), to differentiate between hyphal material and background. The background consisted of the material used for pellet fixation, air between the hyphae, and small impurities.

First, the fixation material was cropped manually with the commercial software VGSTUDIO MAX (version 3.2; Volume Graphics GmbH) or automatically using MATLAB (version 2019b; MathWorks). In the automatic segmentation, the gray level image was first binarised by setting a gray value threshold, which was calculated with Otsu's method (Otsu, 1979). After the binarisation, small connected objects were removed, so that only the sample holder remained as a foreground object in the binarised image. The complement of the binarized image was calculated and multiplied with the original gray level image, resulting in a gray level image without sample holder. Second, the pellets were segmented from each other manually by drawing a region of interest around each pellet with VGSTUDIO MAX or automatically using MATLAB. Therefore, the gray level image without sample holder was binarised by setting a gray value threshold, which was calculated with Otsu's method (Otsu, 1979). The result was a binarised image with the pellets as the foreground object. Furthermore, the binarised pellets were dilated and a watershed segmentation (Meyer, 1994) was performed. The segmented, labeled, and dilated pellet objects were read out successively from the original gray level image with multiple pellets. Finally, the resulting gray level images with only one single pellet were cropped according to the pellet size.

To differentiate between the hyphae and the voids between the hyphae on the cropped gray level images with single pellets, further image processing steps were carried out automatically using MATLAB (version 2019a). *A. niger*, *R. stolonifer*, and *R. oryzae* pellets were binarised by setting a gray value threshold, which was calculated with Otsu's method (Otsu, 1979). However, for *P. chrysogenum* pellets, this method was not sufficient. Therefore, the gray level values were clustered using Gaussian mixture modeling (Bishop, 2009; McLachlan & Peel, 2000) with three classes. To reduce the computational effort, a random sample subset of 10% of the total voxel count was drawn from the image and used for model creation. For the sake of stability, the model was built seven times and the one with the biggest log likelihood was chosen as the final model. Afterwards, all voxels were classified against this model by calculating the largest posterior probability (Bishop, 2009). The three classes represent the gray level values of the background, the noise, and the hyphal material. All gray level values in the class of the hyphal material were set to one, representing the foreground, whereas the gray level values of the other two classes were set to zero, representing the background in the binarised image.

After binarisation, connected objects smaller than or equal to  $5000 \mu\text{m}^3$  for *R. oryzae* and *R. stolonifer* and  $1000 \mu\text{m}^3$  for *P. chrysogenum*, *A. niger* MF19.5, and *A. niger* MF22.4 were deleted, to eliminate small impurities between the hyphae.

Further diffusion computations were conducted with these final processed 3D images of pellets.

## 2.4 | Diameter of hyphae

We used MATLAB (version 2019a) to determine the diameter of the hyphae based on the maximum ball method (Silin & Patzek, 2006). Therefore, we applied euclidean distance transform on the complemented binarised 3D image with hyphae as foreground (MATLAB function "bwdist"). As a result, the closest Euclidean distance of each hyphal voxel to a nonhyphal voxel was stored in the 3D matrix *D* (same dimension as the whole 3D image). Nonhyphal voxels were assigned to zero. In addition, we applied ultimate erosion (MATLAB function "bwulterode") on the binarised 3D image, which resulted in the 3D matrix *E* (same dimension as the whole 3D image), which consisted of the regional maxima of the Euclidean distance transform of the complement of the binarised image. To obtain the regional hyphal diameters within whole pellets, the corresponding elements of *D* and *E* were multiplied. The regional hyphal diameters were used to calculate the arithmetic mean of the hyphal diameter.

## 2.5 | Morphological simulations

Our morphological simulations were based on stochastic growth models for filamentous microorganisms (Celler et al., 2012; Yang et al., 1992) and resulted in 3D images thereof. We implemented the simulations in MATLAB (version 2019a). Video S1 visualizes the growth process of an exemplary noncoagulative pellet from a single spore. In our model, the following fundamental changes were made compared with the model of Celler et al. (2012):

- New in our study: Spore aggregates can be used as initial condition; voxel-based 3D image generation of morphological output that makes the data comparable with  $\mu\text{CT}$  images.
- Neglected in our study: Cross wall-formation; oxygen as a limiting component for growth.

Our model can be divided into three sections: (1) spore aggregation, (2) growth, and (3) generation of 3D structure (Figure 1). In the following, the basics of the three sections are described.

We simulated spore aggregation based on the diffusion-limited aggregation (DLA) method (Witten & Sander, 1983; Figure 1, top). DLA was initialized with a seed spore at the origin of a lattice. The second spore started random walk from far away. The coordinate was fixed if the second spore got in contact with the seed spore. If the distance to the seed spore became too large, later contact would be unlikely and the spore was rejected. The next spore started

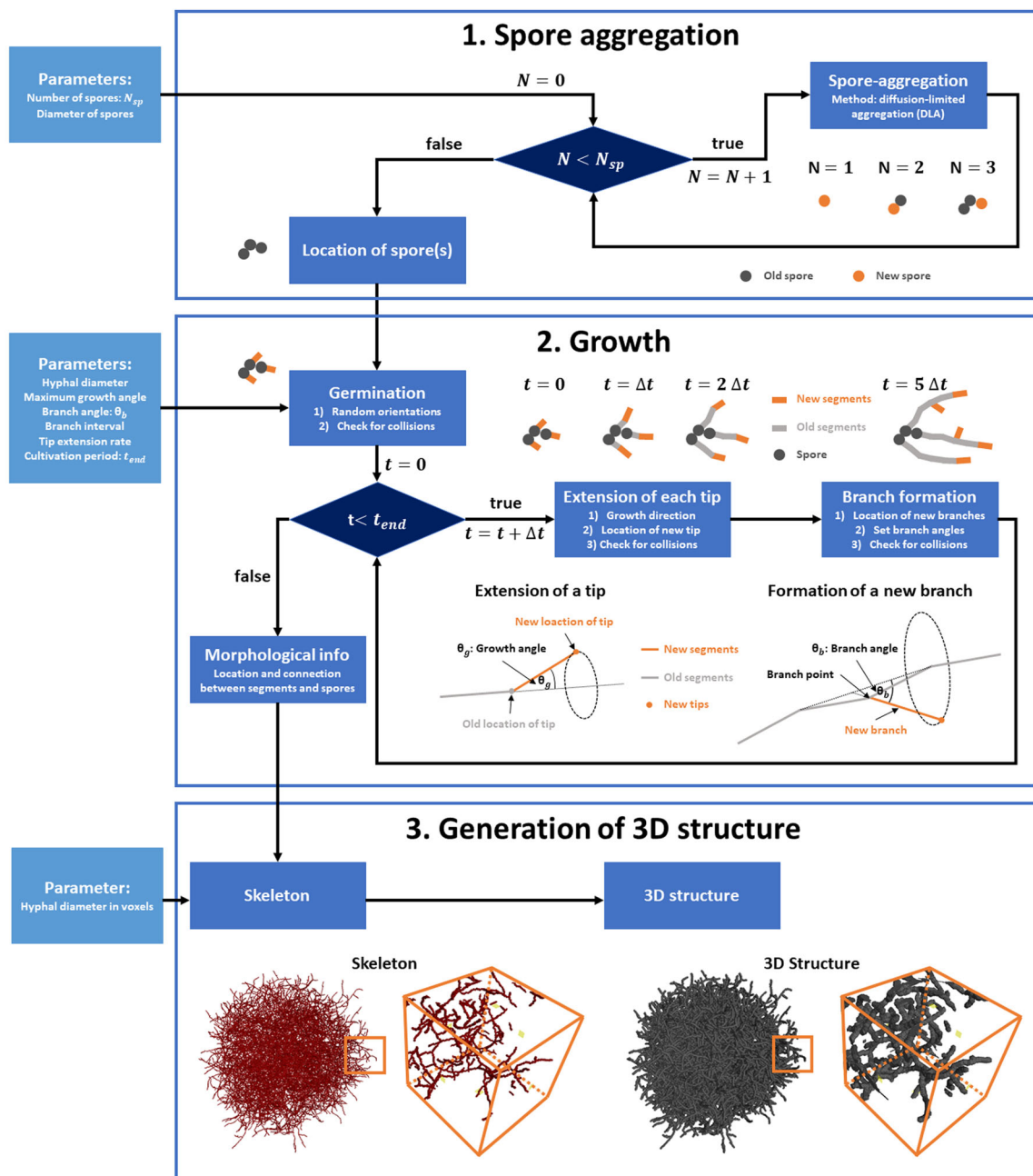


**FIGURE 1** Overview of the algorithm of morphological simulations [Color figure can be viewed at [wileyonlinelibrary.com](http://wileyonlinelibrary.com)]

random walk until it had contact or was too far from the spore aggregate. This procedure was repeated until the desired number of spores  $N_{sp}$  (Table S1) was reached.

Growth was based on the germination of spores, the extension of tips, and the formation of branches (Figure 1, middle). The location of spores served as input for the growth section, where they germinated simultaneously in random orientations forming segments with the length  $l_{germ}$ . Thereby, collisions of germlings with other germlings or spores were prevented. After germination, the extension of tips and the formation of branches started. These two phenomena repeated until the end of the cultivation. Exemplarily, a cultivation period of  $t_{end} = 48\text{h}$  and a time step for calculations  $\Delta t = 0.1\text{h}$  would

result in 480 time steps. In each time step, the extension of each tip is determined. Therefore, a growth angle  $\theta_g$  between  $0^\circ$  and the maximum growth angle is chosen randomly. The length of the new segment  $l_{segment}$  is the product of  $\Delta t$  and the tip extension rate  $\alpha$ . The growth angle and the length of the segment form a circle, whereon the location of the new tip is calculated randomly (Figure 1). The new segment is defined as the connection between the old and the new tip. To prevent overlapping hyphae, possible collisions between the new segment and other segments or spores are detected with closest-point computations (Ericson, 2010). If a collision is detected, the new segment is rejected. However, the same tip is checked for extension in the next calculation step. Similar to Celler et al. (2012),

new branches could be formed in the subapical region of hyphae. The subapical region had a length of  $l_{\text{subapical}}$  and started beginning from the tip (Table S1). In each time step, one possible new branch point (node between two segments, Figure 1) per subapical region was chosen randomly. Before the new branch was generated at this branch point, four conditions had to be fulfilled: (1) location in subapical region, (2) no branches in the neighboring four nodes, (3) current number of branches of the hyphae was lower than the possible number of branches, and (4) no collision of new segment with other segments or spores. The possible number of branches per hyphae was calculated by dividing the length of the hyphae by the minimum mean distance between two branches  $d_{b,\min}$  (Table S1). If conditions one through three were fulfilled, a possible new branch was calculated. The branch angle  $\theta_b$  and the length of the segment  $l_{\text{segment}}$  formed a circle, whereon the location of the tip of the new branch was calculated randomly (Figure 1). Similar to the extension of tips, the new segment was checked for collisions with other segments or spores (Ericson, 2010) and rejected if a collision was detected. Finally, the growth section resulted in morphological information, that is, the location and connection of nodes, hyphal segments, and spores.

The morphological information of the growth section served as input to generate voxel-based 3D structures (Figure 1, bottom). To scale the 3D images, the location of nodes (points between segments or center of spores) was multiplied with the scaling factor  $f_{\text{scale}} = \frac{d_{h,vx}}{d_h}$ , where  $d_{h,vx}$  and  $d_h$  are the hyphal diameters in voxels and  $\mu\text{m}$ , respectively. Varying  $d_{h,vx}$  for the same morphological information generated 3D images of pellets only differing in resolution. To obtain skeletons of pellets, the connections between nodes were discretised based on Bresenham's line algorithm (Bresenham, 1965). Finally, the skeletonized images were dilated using a spherical structuring element to obtain 3D images of pellets with the desired hyphal diameter and resolution.

## 2.6 | Diffusion computations

We computed the continuum diffusion through the voxel-based structures of filamentous pellets gained from both simulations and processed  $\mu\text{CT}$  measurements. Similar to our previous study (Schmideder, Barthel, Müller, et al., 2019), we calculated the diffusive mass transport using the commercial software GeoDict (Becker et al., 2011; Velichko et al., 2009; Math2Market GmbH) that uses the explicit jump finite volume solver by Wiegmann and Zemitis (2006) for diffusion computations. Depending on the size of the pellets, approximately 50–150 representative cubic sub-volumes per pellet were extracted using MATLAB (version 2019a) and further used for diffusion computations (Video S2). An edge length sixfold the hyphal diameter proved to be sufficient as representative elementary volume (REV) of the extracted cubes to fit the parameter  $a$  in  $k_{\text{eff}} = (1 - c_h)^a$  (Figure S1) and to investigate the porosity and diffusivity (Figures S2 and S3). The cubes were selected along the three main axes originating from the calculated mass center of the pellets.

We applied a diffusion computation in the radial direction of each extracted cube, resulting in an effective diffusivity ( $k_{\text{eff}}$ ) in radial direction, that is, the direction pointing to the mass centre of the pellet. In addition, the hyphal fraction ( $c_h$ ) of the cubes, that is, the ratio of volume of hyphae to the total volume, was analyzed. Similar to our previous study (Schmideder, Barthel, Müller, et al., 2019), the diffusion computations were conducted in the liquid between the hyphae, the porous medium. Pure bulk diffusion was assumed, because it is the predominant diffusion regime in liquids (Becker et al., 2011; Panerai et al., 2017). In our study we neglected surface effects on the solid-liquid interface that could influence diffusion (Schmideder, Barthel, Müller, et al., 2019). The diffusion was modeled by the Laplace equation, with Neumann boundary conditions on the pores-to-solids boundaries, and a concentration drop of the diffusing component in the diffusion direction (Becker et al., 2011). In addition, we applied Dirichlet boundary conditions on the in- and outlet and symmetric boundary conditions on the other four faces.

## 3 | RESULTS AND DISCUSSION

### 3.1 | Correlation of morphology and diffusive mass transport in $\mu\text{CT}$ -measured pellets

Because pellet morphology is, inter alia, strain dependent, we investigated five different strains from four fungal cell factories: *P. chrysogenum* (penicillin producer); *A. niger* (citric acid and enzyme producer, with one isolate displaying wildtype morphology; strain MF19.5), and one hyperbranching isolate (strain MF22.4; Fiedler et al., 2018); *R. stolonifer* (fumaric acid); and *R. oryzae* (enzymes, tempeh). At least three pellets per strain were analyzed by  $\mu\text{CT}$ , which allows non-destructive 3D investigations of intact pellets (Schmideder, Barthel, Friedrich, et al., 2019). The 3D morphology and an exemplary diffusion computation through a *R. stolonifer* pellet are shown in Video S2.

Remarkably, pellet morphologies were highly diverse among the strains (Figure 2). Equatorial slices of pellets showed that the distribution of hyphal material ranged from nearly spherically symmetric (*R. oryzae*, *R. stolonifer*, and *A. niger*) to a distribution far from spherical symmetry (*P. chrysogenum*). The porosity within the pellets also differed significantly. For example, *R. stolonifer* pellets had a loose structure whereas *A. niger* pellets were much denser. In addition, the porosity varied from nearly homogeneous (*A. niger* MF22.4 and *R. stolonifer*) to strongly heterogeneous (*R. oryzae* and *P. chrysogenum*). The mean hyphal diameter of *P. chrysogenum*, *A. niger* MF19.5, *A. niger* MF22.4, *R. stolonifer*, and *R. oryzae* was 4.3, 4.0, 4.3, 8.3, and 4.5  $\mu\text{m}$ , respectively. Although the morphology of the investigated strains varied strongly, the results of the diffusion computations were surprisingly very similar (Figure 2, bottom row). The correlation

$$k_{\text{eff}} = (1 - c_h)^a \quad (2)$$

between the effective diffusion factor ( $k_{\text{eff}}$ ) and the hyphal fraction ( $c_h$ , ratio of hyphal material inside the cubes) fitted well for all strains.

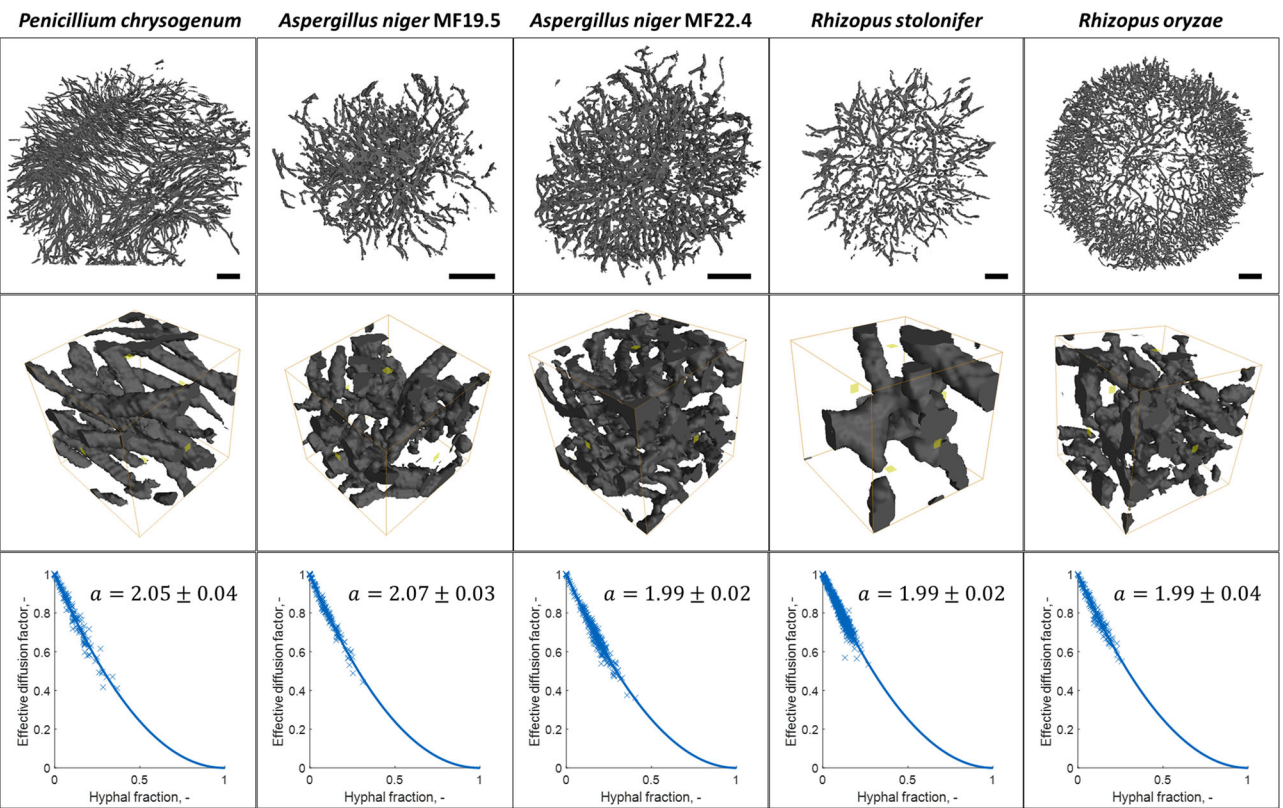


**FIGURE 2** Morphology and diffusivity of experimentally investigated pellets. Upper two rows: Exemplary projections of processed three-dimensional microcomputed tomography ( $\mu$ CT) images. Slices are from equatorial regions with a depth of 30  $\mu$ m. Cubes are 50  $\times$  50  $\times$  50  $\mu$ m. Bottom row: correlation between hyphal fraction ( $c_h$ ) and effective diffusion factor ( $k_{eff}$ ). Each blue data point corresponds to one cube applied for diffusion computations. The solid blue line is the correlation between the hyphal fraction and the effective diffusion factor, resulting in the fitted exponent  $a$  in (Schmideder, Barthel, Müller, et al., 2019):  $k_{eff} = (1 - c_h)^a$ .  $\pm$  specifies the 95% confidence interval.  $\mu$ CT measurements were conducted with a voxel size of 1  $\mu$ m (three *Penicillium chrysogenum*, three *Aspergillus niger* MF19.5, five *A. niger* MF22.4, and three *Rhizopus oryzae* pellets) and 2  $\mu$ m (11 *R. stolonifer* pellets). For each strain, at least 149 cubes were investigated. Scale bar: 100  $\mu$ m [Color figure can be viewed at [wileyonlinelibrary.com](http://wileyonlinelibrary.com)]

The correlation is known as Archie's law with a cementation parameter equal to  $a$  (Archie, 1942) and was already applied for one *A. niger* strain in our previous study (Schmideder, Barthel, Müller, et al., 2019). Including the 95% confidence interval, the exponent  $a$  was  $2.05 \pm 0.04$ ,  $2.07 \pm 0.03$ ,  $1.99 \pm 0.02$ ,  $1.99 \pm 0.02$ , and  $1.99 \pm 0.04$  for *P. chrysogenum*, *A. niger* MF19.5, *A. niger* MF22.4, *R. stolonifer*, and *R. oryzae*, respectively.

The similarity of the diffusion laws raises the issue of a generalized law for filamentous fungi. However, as there are an estimated six million fungal species on earth (Taylor et al., 2014), many of them filamentous and capable of forming numerous different morphologies (Cairns et al., 2019), our  $\mu$ CT-based experimental approach is not target orientated to investigate a generalized law.

### 3.2 | Correlation of morphology and diffusive mass transport in simulated pellets

To determine a generalized law for the diffusivity through fungal pellets that would be applicable to any filamentous fungus of interest,

we decided to follow an unbiased modeling approach. Using a Monte Carlo growth model (Celler et al., 2012; see Section 2), we thus simulated a huge variety of pellet morphologies and then exposed the simulated pellets to diffusion computations (see Section 2 and Video S2).

In the morphological simulations, both the coagulative and noncoagulative fungal spore aggregation phenomena (Metz & Kossen, 1977; Zhang & Zhang, 2016) were taken into account. In brief, a coagulative pellet forms by aggregation of hundreds to thousands of spores before they start to germinate, and a non-coagulative pellet could form from the germination of a single spore (Cairns et al., 2019). For the former case, we decided to model the aggregation of spores by diffusion-limited aggregation (Witten & Sander, 1983; see Section 2). Figure 3 highlights that the unbiased morphological simulations indeed enabled the development of both coagulative and noncoagulative pellet types, which reasonably matched the experimental data for the coagulative *A. niger* MF19.5 and the noncoagulative *R. stolonifer*, respectively. The growth process of a non-coagulative pellet is shown in Video S1.

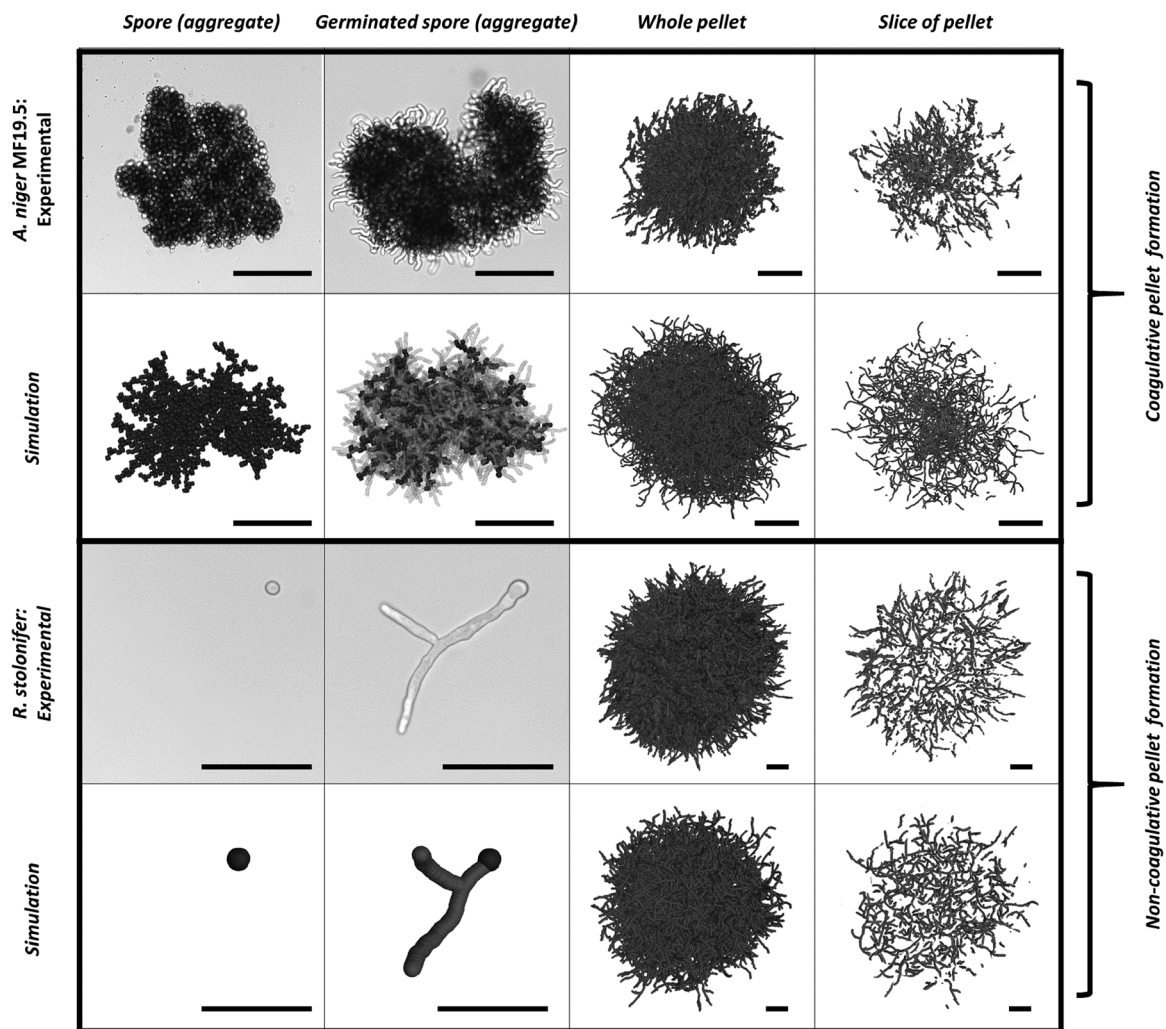


**FIGURE 3** Experimental and simulated coagulative and noncoagulative pellet formation. First and third rows show experimental data of coagulative pellet forming *Aspergillus niger* MF19.5 (Fiedler et al., 2018) and noncoagulative pellet forming *Rhizopus stolonifer*, respectively. Second and fourth rows illustrate simulations of coagulative and noncoagulative pellet formation, respectively. First column shows spore (aggregates), second column germinated spore (aggregates), third column two-dimensional (2D) projections of three-dimensional (3D) pellets, and fourth column slices of pellets with a depth of 30 µm. Images of experimental spore aggregates were captured with light microscopy, whereas experimental pellets were measured with microcomputed tomography ( $\mu$ CT) to determine 3D images. Spore aggregation of coagulative pellet formation was simulated with the diffusion-limited aggregation method (Witten & Sander, 1983) and 2048 spores. Pellet growth was simulated with the Monte Carlo model described in Section 2. Scale bar: 100 µm

Pellet formation is not only dependent on coagulative and noncoagulative spore aggregation type but also on the genetic make-up of the species and process-relevant parameters (Cairns et al., 2019). To simulate a broad range of morphologically different pellets, our simulation therefore considered high variation of five morphological parameters (Figure 4): maximum growth angle, branch angle, hyphal diameter, branch interval, and number of initial spores. For each of these parameters, five values were estimated, resulting in  $5^5 = 3125$  morphologically different structures in total. In a recent study (Lehmann et al., 2019), the investigation of 31 filamentous fungal species resulted in mean branching angles between  $26^\circ$  and  $86^\circ$ , mean internodal lengths (distance between two branches) between 40 and 453 µm, and mean hyphal diameters between 2.7 and 6.5 µm. However, the diameter of fungal hyphae has been reported to range from 2

to 10 µm (Meyer et al., 2020; Zucchetti et al., 2018). We decided to also consider in the simulations the hyphal diameter of filamentous bacteria (about 0.5–1 µm), as filamentous bacteria are morphologically similar to filamentous fungi (Nielsen, 1996; Zucchetti et al., 2018), with *Streptomyces* as important cell factories for antibiotic production (Nepal & Wang, 2019). In our simulations, the parameter branch angle was set to  $20^\circ$ ,  $55^\circ$ ,  $90^\circ$ ,  $125^\circ$ , or  $160^\circ$ , whereby angles larger than  $90^\circ$  orient the branch towards the opposite direction of the leading hyphae. The morphological parameter branch interval was defined as the ratio between the internodal length and the hyphal diameter, scaled with the hyphal diameter because large internodal lengths are linked with large hyphal diameters (Lehmann et al., 2019). As expected, simulations with large branch intervals produced disperse mycelia instead of pellets. Thus, we set the maximum branch interval

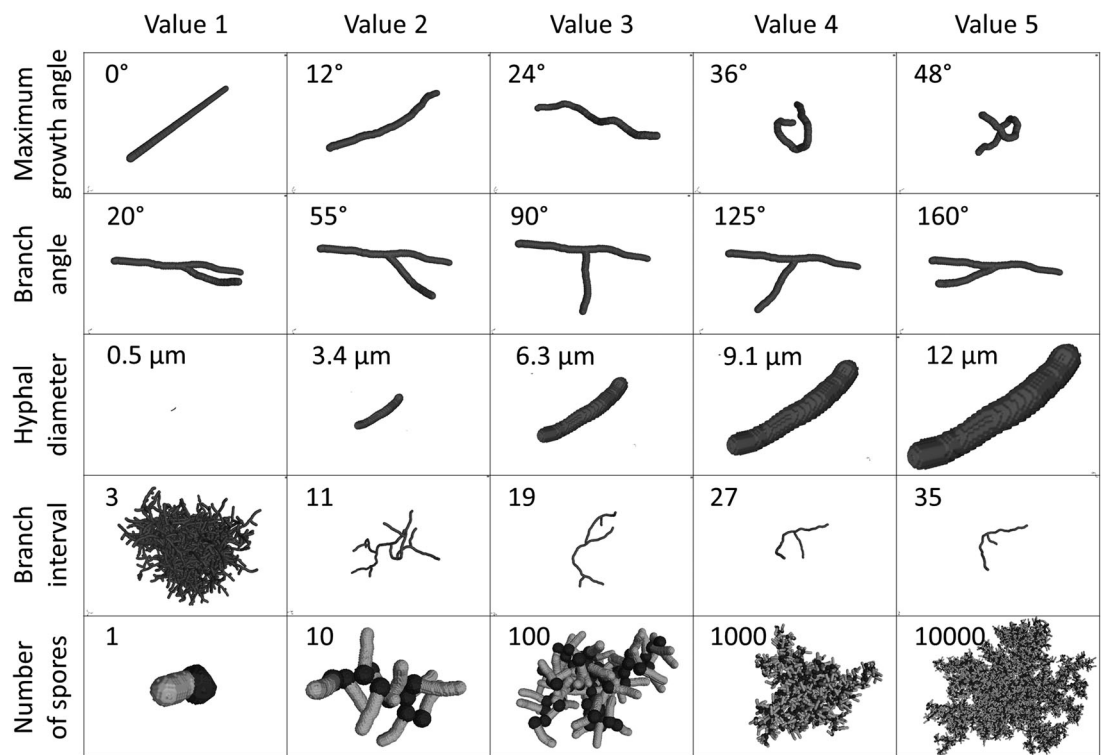


**FIGURE 4** Applied morphological parameters for simulations of filamentous structures. Five morphological parameters were applied: maximum growth angle, branch angle, hyphal diameter, branch interval (ratio between the distance between two branches and the hyphal diameter), and number of initial spores. Each of these parameters was varied to five values resulting in a total of  $5^5 = 3125$  simulations performed with the Monte Carlo method described in Section 2

to 35. The maximum number of initial spores was set to 10,000 because coagulative pellets can result from hundreds or thousands of agglomerated spores (Fontaine et al., 2010; Metz & Kossen, 1977). Due to the lack of literature describing the growth angle of hyphae, we varied the maximum growth angle within a range to consider straight growing ( $0^\circ$ ) and strongly curved ( $48^\circ$ ) hyphae.

Our Monte Carlo simulations covered a broad morphological range of filamentous fungal pellets, which we believe also includes pellets reflecting macromorphologies from smaller filamentous bacteria.

Because image resolution could influence computed properties (Schmideder, Barthel, Müller, et al., 2019; Velichko et al., 2009), we further investigated the influence of pellet resolution on their diffusivity. In Figure 5a, an exemplary cube of a simulated pellet is shown that differs only in resolution, that is, the number of voxels that span a given hyphal diameter. In this figure, the image resolution increases from top to bottom, and the hyphae appear more cylindrical. Notably, the  $\alpha$  value in  $k_{eff} = (1 - c_h)^\alpha$  decreases with increasing resolution of three exemplary simulated pellets and converges to  $1.6 < \alpha < 1.8$ , suggesting that the  $\alpha$  value converges with increasing resolution.

To investigate the influence of the image resolution of experimentally determined pellets on their diffusivity, we thus conducted µCT measurements with different resolutions. In particular, *R. stolonifer* pellets were measured with a voxel size of 1, 2, 3, and 4  $\mu\text{m}$  and

*R. oryzae* pellets with a voxel size of 1 and 2  $\mu\text{m}$ . The decrease in the voxel size led to an increased resolution. Similar to simulated pellets,  $\alpha$  in  $k_{eff} = (1 - c_h)^\alpha$  decreased with increasing resolution (Figure 5b). Note that (i) measurements with a voxel size of 1  $\mu\text{m}$  in the case of *R. stolonifer*, the organism with the highest hyphal diameter in this study, result in hollow hyphae (Figure S4), which cannot be used for diffusion computations and (ii) that low resolutions result in coarse surfaces of the hyphae that do not reflect their smooth nature. Thus, 3D images of filamentous pellets are limited to a minimum and maximum resolution for each organism, which strongly depends on their hyphal diameters. We therefore propose the application of an image resolution that represents hyphae with about four to six voxels in diameter.

Tomadakis and Robertson (2005) summarized and extended correlations between the morphology and the diffusivity, conductivity, and permeability through fiber structures with different orientations. The study was based on previous studies by Tomadakis & Sotirchos, (1991, 1993, 1993, 1993). To validate our diffusion computations and to identify an appropriate resolution for simulated pellets, we compared the solution for randomly orientated overlapping straight fibers by Tomadakis and Sotirchos (1991) with our computed diffusivity through such a morphology. We set up a simulation with 1000 spores, a growth angle of  $0^\circ$ , and allowed collisions (Figure 6a) to obtain randomly orientated overlapping straight fibers. As shown in Figure 6b,c, our simulated structure was

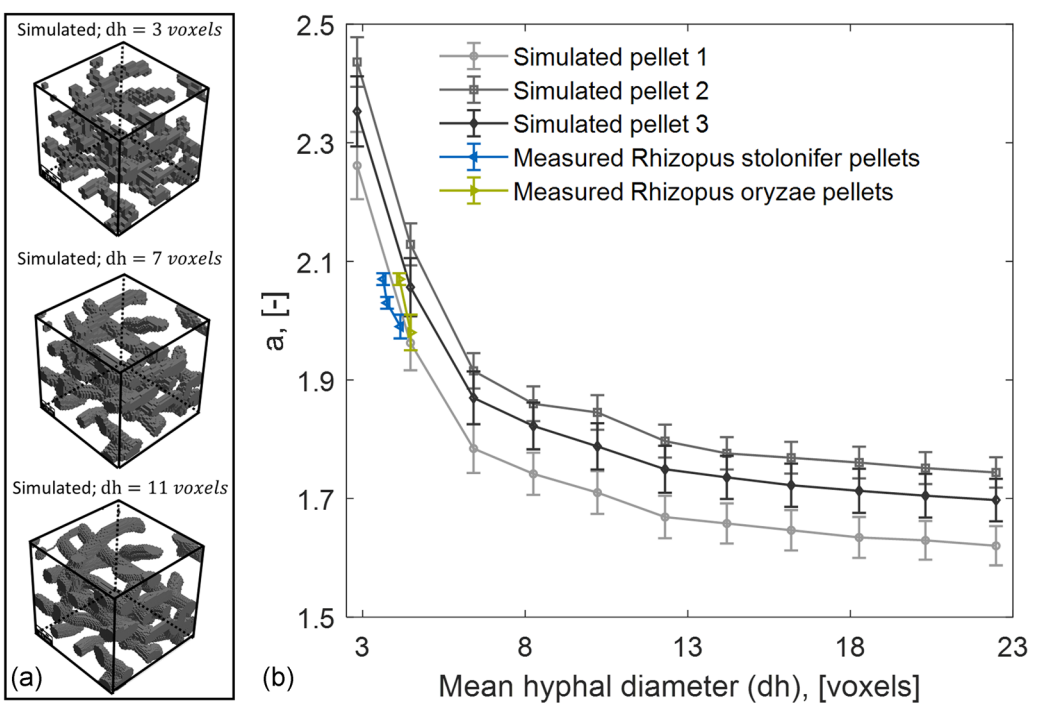


**FIGURE 5** Relationship between image resolution and effective diffusivity. Image resolution is represented by the number of voxels that span a given hyphal diameter. Left: Identical exemplary cube of a simulated pellet that differs only in image resolution. Exemplarily, hyphae are represented with 3, 7, and 11 voxels in diameter. Right:  $a$  value of experimentally determined pellets and three exemplary simulated pellets fitted on a base of at least 37 cubes per pellet with  $k_{eff} = (1 - c_h)^a$ , where  $k_{eff}$  is the effective diffusion factor,  $c_h$  the hyphal fraction, and  $a$  the fitted correlation factor (Schmideder, Barthel, Müller, et al., 2019). Morphological simulations of pellets were performed with the Monte Carlo method described in the Section 2. *Rhizopus* pellets were measured with microcomputed tomography ( $\mu$ CT) with a voxel size of 1  $\mu$ m (three *R. oryzae* pellets), 2  $\mu$ m (21 *R. oryzae* and 11 *R. stolonifer* pellets), 3  $\mu$ m (13 *R. stolonifer* pellets), and 4  $\mu$ m (seven *R. stolonifer* pellets). Each data point of measured pellets was fitted on the base of cubes of the mentioned number of pellets. Error bars specify the 95% confidence interval [Color figure can be viewed at [wileyonlinelibrary.com](http://wileyonlinelibrary.com)]

comparable to the structure used for the correlation  $k_{eff} = \epsilon \left( \frac{\varepsilon - 0.037}{1 - 0.037} \right)^{0.661}$  (Tomadakis & Sotirchos, 1991). With increasing resolution, that is, with increasing voxels representing the hyphal diameter, the computed diffusivities of the simulated structure approached the correlation of Tomadakis and Sotirchos (1991; Figure 6d). Especially in the hyphal fraction range 0–0.4, our computed diffusivities fit well with their correlation, suggesting that the diffusion computations were accurate for high resolutions in the hyphal fraction range 0–0.4. The range reflects the hyphal fraction of both simulated and experimentally determined pellets (Figures 2 and 7, see next Section 3.3).

### 3.3 | Merging diffusive mass transport data from simulated and $\mu$ CT measured pellets

We investigated the diffusive mass transport in filamentous fungal mycelia through the correlation between the diffusivity and morphology of 3125 simulated and 66  $\mu$ CT analyzed pellets. We applied an image resolution that represented simulated hyphae five voxels in diameter to make the results of simulations and experiments comparable (Figure 7a). Because this resolution could underestimate the

diffusivity (Figure 6 and our previous study; Schmideder, Barthel, Müller, et al., 2019), we also applied a resolution that represented hyphae with 13 voxels in diameter (Figure 7b). We considered this resolution as a compromise between accuracy and computational effort of diffusion computations. Similar to experimentally determined pellets, we used several cubes of each simulated structure for diffusion computations.

Interestingly, pellet formation did not occur for all parameter combinations. The combination of low spore numbers and rare branches resulted in dispersed mycelia instead of pellets. Thus, we marked loose structures with a mean hyphal fraction of the respective cubes less than 0.05. As a result, the initial 3125 simulated structures were reduced to 1280 and 1791 pelletised structures for hyphae represented with 5 and 13 voxels, respectively (Figure 7). The mean correlation factor  $a \pm \sigma(a)$  of all 3125 structures was  $a = 2.059 \pm 0.182$  and  $a = 1.757 \pm 0.150$  for hyphae represented with 5 and 13 voxels, respectively (Figure 7, top and bottom). For pelletized structures, the mean was altered to  $a = 2.063 \pm 0.044$  and  $a = 1.753 \pm 0.035$ , respectively. In Figure 7, pellets with unlikely morphological parameters were marked, namely all pellets with straight hyphae (maximum growth angle = 0°) or extreme branch angles (branch angle = 20° and branch angle = 160°). Thus, the

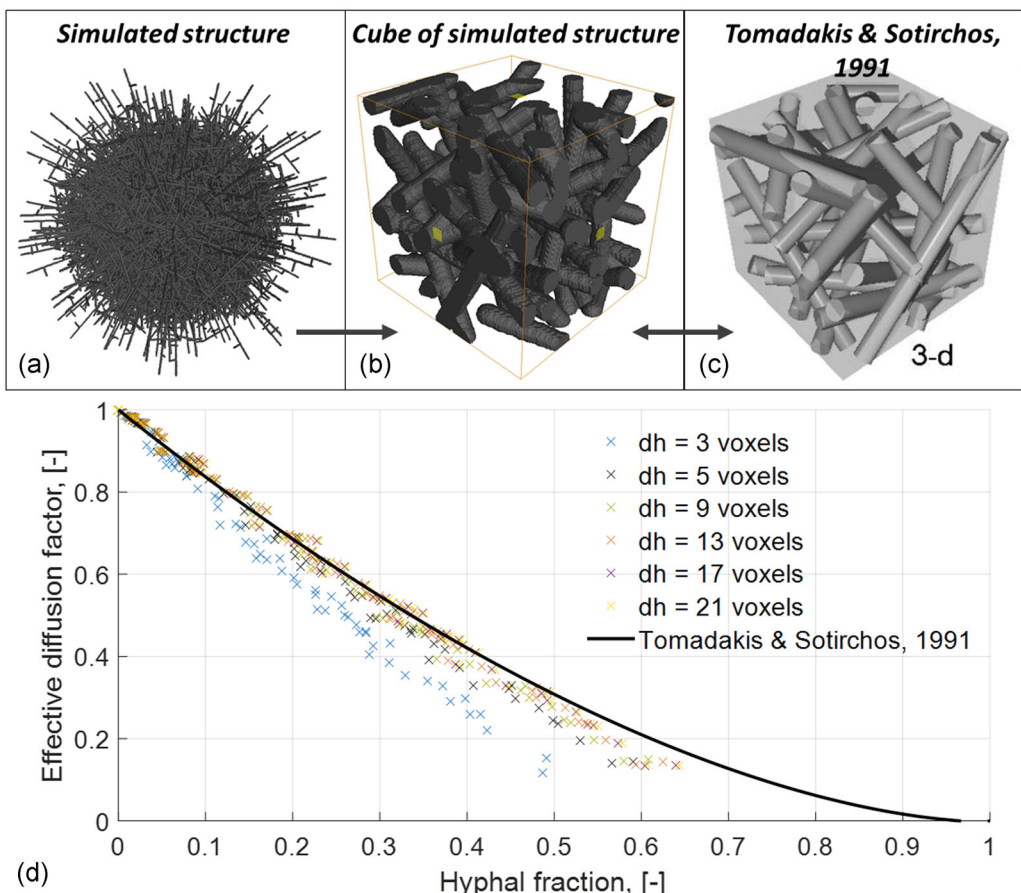


**FIGURE 6** Validation of diffusion computations. The solution for the effective diffusion factor  $k_{eff}$  through randomly orientated overlapping straight fibers  $k_{eff} = \varepsilon \left( \frac{\varepsilon - 0.037}{1 - 0.037} \right)^{0.661}$  by Tomadakis and Sotirchos (1991) was compared with the computed  $k_{eff}$  through similar simulated structures. The porosity was  $\varepsilon = 1 - \text{hyphal fraction}$ . We performed the morphological simulations with the Monte Carlo method described in the Methods section. (a) Whole simulated structure. (b) Exemplary cube of simulated structure. For diffusion computations, 76 cubes were investigated for each resolution. Resolution is represented by the number of voxels that spanned the given hyphal diameter. (c) Model structure applied for solution by Tomadakis and Sotirchos (1991). (d) Solution by Tomadakis and Sotirchos (1991) (black line) and computed diffusivities through simulated structure. Each data point corresponds to the diffusivity through one cube [Color figure can be viewed at [wileyonlinelibrary.com](http://wileyonlinelibrary.com)]

number of pellets was reduced to 898 and 712, with a narrow distribution of the correlation factor  $a = 2.072 \pm 0.025$  and  $a = 1.760 \pm 0.023$  for hyphae represented with 5 and 13 voxels in diameter, respectively. Pellets with unlikely morphological parameters explain the outliers for the correlation factor  $a$ . For the experimentally determined pellets of *P. chrysogenum*, *A. niger* MF19.5, *A. niger* MF22.4, *R. stolonifer*, and *R. oryzae*,  $a$  was 2.05, 2.07, 1.99, 1.99, and 1.99 (Figure 2), respectively, and thus in the range of the simulated pellets where the hyphae are represented with 5 voxels in diameter (Figure 7, top). Applying the maximum ball method (Section 2), this is a mean hyphal diameter of 4.5 voxels that lies in the range of our experimental pellets (4.3, 4.0, 4.3, 4.2, and 4.5 voxels for the different strains).

The results strongly indicate that the diffusion law  $k_{eff} = (1 - c_h)^a$  is applicable to fungal pellets with arbitrary morphology. In addition, the only fitting parameter  $a$  lies in a narrow range while the resolution of the images does not change. This implies that there is a

generalizable law for the diffusivity through fungal pellets with the hyphal fraction  $c_h$  as the only independent variable. Contrary to our expectations, detailed morphological parameters such as growth angles, branch angles, hyphal diameters, number of initial spores, and branching frequency did not affect the diffusive hindrance. For all 3125 simulated pellets we applied image resolutions to represent the hyphal diameter with 5 and 13 voxels, respectively. We were able to show that low resolutions (Figure 7a) lead to an underestimation of the diffusivity (Figure 6 and our previous study; Schmideder, Barthel, Müller, et al., 2019). In addition, the results of three simulated pellets with different image resolutions (Figure 5b) show that the  $a$  parameter converges with increasing resolution for each pellet. Thus, we suggest to use the law for high resolutions (the hyphal diameter is represented with 13 voxels in diameter; Figure 7b) to calculate the diffusivity through fungal pellets:

$$k_{eff} = (1 - c_h)^{1.76} \quad (3)$$

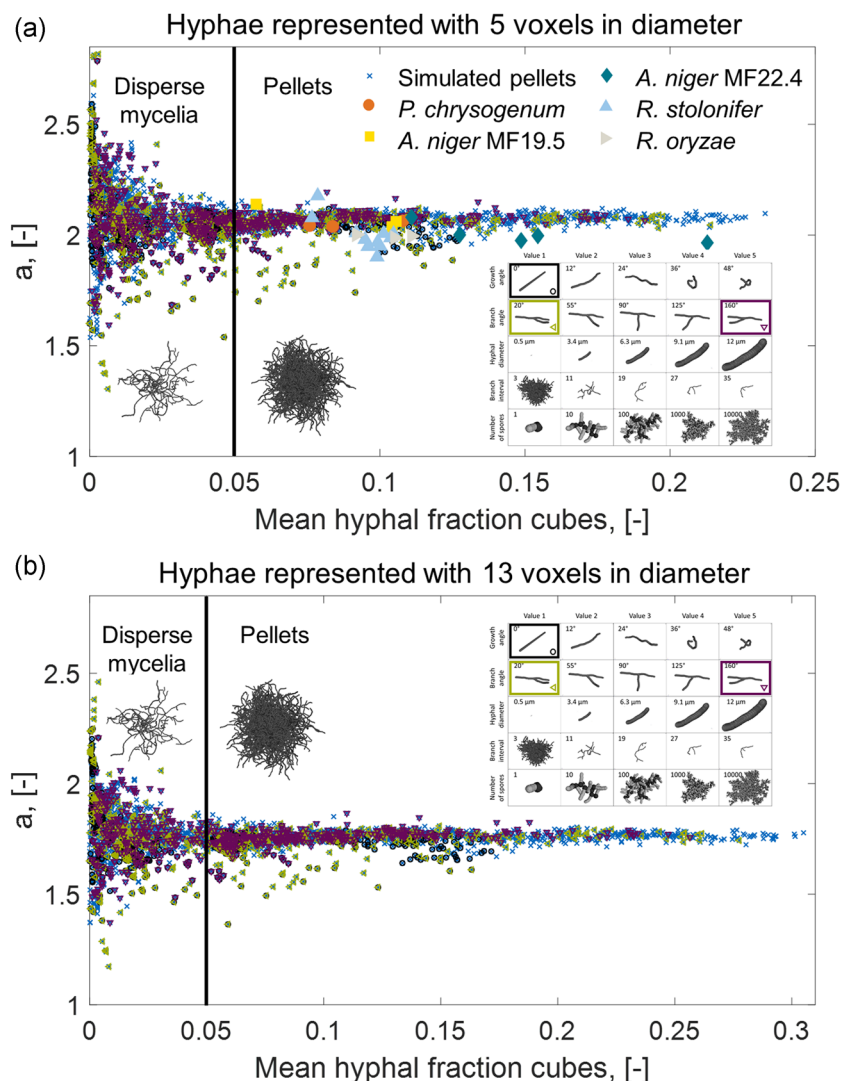


**FIGURE 7** Correlation factor  $a$  for simulated and experimentally determined pellets. Each data point corresponds to the correlation between the hyphal fraction  $c_h$  and the effective diffusion factor  $k_{eff}$  of one pellet, resulting in the fitted exponent  $a$ . For each pellet, the fit is based on diffusion computations through several cubes and the correlation  $k_{eff} = (1 - c_h)^a$ . Hyphae of simulated pellets are represented with a “resolution” of five (top) and 13 (bottom) voxels in diameter. The increasing resolution decreases the correlation factor  $a$ , and thus the diffusivity decreases as well. Morphological simulations for diffusion computations of simulated pellets were performed with the Monte Carlo method described in the Section 2. Microcomputed tomography ( $\mu$ CT) measurements for diffusion computations of experimentally determined pellets were conducted with a voxel size of  $1 \mu\text{m}$  (three *Penicillium chrysogenum*, three *Aspergillus niger* MF19.5, five *A. niger* MF22.4, three *Rhizopus oryzae* pellets), and  $2 \mu\text{m}$  (11 *R. stolonifer* pellets) [Color figure can be viewed at [wileyonlinelibrary.com](https://wileyonlinelibrary.com)]

where  $k_{eff}$  is the effective diffusion factor ( $k_{eff}^{-1}$  is similar to the formation factor) describing the geometrical diffusion hindrance through a 3D structure, and  $c_h$  is the hyphal fraction (similar to solid fraction). As shown in Figure S5, our law is not very distinct from the law of random orientated overlapping fibers by Tomadakis and Sotirchos (1991). However, our correlation differs very strongly from the correlation for random orientated overlapping fibers proposed by He et al. (2017). For low porosities, the correlation of He et al. (2017) proposes effective diffusion factors larger than 1, which is physically unreasonable. It has to be mentioned that our law might slightly underestimate the diffusivity through filamentous fungal networks, because Figure 5 implies that the convergence might not be fully developed for a resolution of 13 voxels. However, doubling the resolution increases the volume of pellets and cubes for diffusion computations eightfold. The increase of the cube-volumes would result in excessive computational times (With a resolution of 13 voxels, the diffusion computations of all 3125 pellets last about 3 weeks with an Intel Xeon E5-1660 CPU (3.7 GHz)). In addition, some pellets could not be reconstructed with very high resolutions because

they would result in working memories larger than our available 128 GB. Thus, the resolution of 13 voxels was a compromise between accuracy and computational effort/feasibility.

## 4 | CONCLUSIONS

This study showed that a universal law (see Equation 3) holds for the diffusive transport of nutrients, oxygen, and secreted metabolites through any filamentous fungal pellet. As mentioned above, the correlation is also known as Archie's law (Archie, 1942) with a cementation parameter equal to 1.76, which is in the range of porous rocks (Glover et al., 1997, e.g., determined that the cementation parameter of sandstone is between 1.5 and 2.5). Strictly speaking, our law is valid for hyphal fractions less than 0.4 because the maximum hyphal fraction of simulated and measured pellets was 0.4. However, to the best of our knowledge, there are no studies about filamentous fungi where the measured hyphal fraction is more than 0.4. For example, Cui et al. (1997, 1998) reported average hyphal

fractions between 0.07 and 0.30 for whole *A. awamori* pellets. If future studies are confronted with hyphal fractions more than 0.4, we propose to fall back on the correlation for randomly orientated overlapping fibers proposed by Tomadakis and Sotirchos (1991), which is (as already stated) not very distinct from our correlation. They were able to show that their correlation was valid for solid fractions less than 0.6, whereas higher solid fractions resulted in another correlation. Our law predicts that only one independent variable, the hyphal fraction ( $c_h$ ), affects pellet diffusivity. Knowing the profile of the hyphal fraction in pellets, the law  $k_{eff} = (1 - c_h)^{1.76}$  determines the mass transport of molecules inside pellets. Molecule concentrations inside pellets are affected by metabolic rates and the transport through filamentous mycelia (Celler et al., 2012; Cui et al., 1998). As the transport can now be calculated, the estimation of metabolic rates within pellets becomes, for the first time, feasible. Future experiments should provide information about the morphology and metabolic activity or nutrient profiles of pellets, which can be, for example, measured through flow cytometry or confocal laser scanning microscopy (Schrinner et al., 2020; Tegelaar et al., 2020; Veiter & Herwig, 2019). One possibility to determine the distribution of oxygen and hyphal material inside pellets would be the application of microelectrodes inside pellets (Hille et al., 2005; Wittier et al., 1986) followed by  $\mu$ CT measurements (Schmideder, Barthel, Friedrich, et al., 2019).

This generalized law was deduced from experimental and simulation data. On the one hand, it proved the usefulness and power of laboratory  $\mu$ CT systems to investigate the natural 3D morphology of different filamentous fungi in utmost detail. However, as this method is time and cost intensive and only applicable to a small number of pellets, the use of Monte Carlo simulations proved to be powerful for the massive generation of data covering a broad range of morphological characteristics. This computational approach allowed us to generate a database of 3125 morphologically different pellets, which will also open up new avenues of research. Such a database, which can be accessed by the community, could also open new paths towards parameter estimation of measured pellets of fungal or bacterial origin. Conclusions about the evolution of measured pellets could be deduced because growth and morphological parameters of simulated pellets are known.

We furthermore anticipate that this contribution will inspire more sophisticated correlation measurements between morphology and mass transport in any complex material, for example, in biofilms, fiber materials, porous media, and fuel cells. In fact, correlations between the morphology and transport properties (Archie, 1942; Carman, 1937; Epstein, 1989; Kozeny, 1927) are crucial to compute transport phenomena in several fields. Exemplarily, correlation laws for fibrous materials (He et al., 2017; Tamayol et al., 2012; Tomadakis & Robertson, 2005) are already applied to design nano- and microporous membranes (Yuan et al., 2008), heat insulations (Panerai et al., 2017) and dissipations (Jung et al., 2016), acoustic insulations (Tang & Yan, 2017), electrodes (Kim et al., 2019), and batteries (Ke et al., 2018). Concerning fibrous materials, a direct link to our study was shown (Figure 6). For nonfibrous materials, a combination of 3D

image acquisition, morphological simulations, and mass transport computations could significantly enhance the understanding of morphology-dependent transport phenomena. Hence, we foresee that the biological and computational approach followed in this study may be synergistically adopted to other research questions in bio(techno)logy and beyond.

## ACKNOWLEDGMENTS

Special thanks go to Katherina Celler and Gilles P. van Wezel and his chair who provided the code used in their study (Celler et al., 2012). The authors thank The Anh Baran for preliminary studies on the morphological simulations, Clarissa Schulze and Michaela Thalhammer for assistance with  $\mu$ CT measurements, Andrea Pape for preparation of pellets, Vincent Bürger for the preliminary code for diffusion-limited aggregation, and Markus Betz and Christian Preischl for preliminary studies on diffusion computations. We also wish to thank Christoph Kirse, Michael Kuhn, Johann Landauer, Thomas Riller, and Johannes Petermeier for helpful and fruitful discussions. This study made use of equipment that was funded by the Deutsche Forschungsgemeinschaft (DFG, German Research Foundation)-198187031. The authors thank the Deutsche Forschungsgemeinschaft for financial support for this study within the SPP 1934 DiSPBiotech-315384307 and 315305620 and SPP2170 InterZell-427889137. Open access funding enabled and organized by Projekt DEAL.

## CONFLICTS OF INTEREST

The authors have no conflicts of interest to declare.

## AUTHOR CONTRIBUTIONS

Stefan Schmideder did the conception and design of the study. Stefan Schmideder, Henri Müller, and Lars Barthel wrote the manuscript, which was edited and approved by all authors. Heiko Briesen and Vera Meyer supervised the study. Lars Barthel and Ludwig Niessen cultivated filamentous fungi and prepared pellets for microcomputed tomography ( $\mu$ CT) measurements. Henri Müller and Stefan Schmideder performed  $\mu$ CT measurements of pellets. Stefan Schmideder, Henri Müller, and Tiaan Friedrich performed image analysis. Stefan Schmideder and Tiaan Friedrich set up the code for morphological Monte Carlo simulations. Stefan Schmideder performed the diffusion computations and analyzed the results.

## DATA AVAILABILITY STATEMENT

The data that support the findings of this study are available from the corresponding author upon reasonable request.

## ORCID

- Stefan Schmideder  <http://orcid.org/0000-0003-4328-9724>
- Henri Müller  <https://orcid.org/0000-0002-4831-0003>
- Lars Barthel  <https://orcid.org/0000-0001-8951-5614>
- Tiaan Friedrich  <https://orcid.org/0000-0001-8346-4908>
- Ludwig Niessen  <https://orcid.org/0000-0003-4083-2779>
- Vera Meyer  <https://orcid.org/0000-0002-2298-2258>
- Heiko Briesen  <https://orcid.org/0000-0001-7725-5907>

## REFERENCES

- Archie, G. E. (1942). The electrical resistivity log as an aid in determining some reservoir characteristics. *Transactions of the AIME*, 146(01), 54–62. <https://doi.org/10.2118/942054-G>
- Becker, J., Wieser, C., Fell, S., & Steiner, K. (2011). A multi-scale approach to material modeling of fuel cell diffusion media. *International Journal of Heat and Mass Transfer*, 54(7–8), 1360–1368. <https://doi.org/10.1016/j.ijheatmasstransfer.2010.12.003>
- Bennet, J. W., & Lasure, L. L. (1991). *More Gene Manipulations in Fungi*. Academic Press.
- Bishop, C. M. (2009). *Pattern Recognition and Machine Learning (Corrected at 8th printing 2009)*. Information science and statistics. Springer.
- Brakhage, A. A. (2013). Regulation of fungal secondary metabolism. *Nature Reviews Microbiology*, 11(1), 21–32. <https://doi.org/10.1038/nrmicro2916>
- Bresenham, J. E. (1965). Algorithm for computer control of a digital plotter. *IBM Systems Journal*, 4(1), 25–30. <https://doi.org/10.1147/sj.41.0025>
- Cairns, T. C., Zheng, X., Zheng, P., Sun, J., & Meyer, V. (2019). Moulding the mould: Understanding and reprogramming filamentous fungal growth and morphogenesis for next generation cell factories. *Biotechnology for Biofuels*, 12(1), 77. <https://doi.org/10.1186/s13068-019-1400-4>
- Carman, P. C. (1937). Fluid flow through granular beds. *Transactions of the Institution of Chemical Engineers*, 15, 150–166.
- Celler, K., Picioreanu, C., van Loosdrecht, Mark, C. M., & van Wezel, G. P. (2012). Structured morphological modeling as a framework for rational strain design of *Streptomyces* species. *Antonie Van Leeuwenhoek*, 102(3), 409–423. <https://doi.org/10.1007/s10482-012-9760-9>
- Cui, Y. Q., van der Lans, R., & Luyben, K. (1997). Effect of agitation intensities on fungal morphology of submerged fermentation. *Biotechnology and Bioengineering*, 55(5), 715–726. [https://doi.org/10.1002/\(SICI\)1097-0290\(19970905\)55:5<715::CO;2-E](https://doi.org/10.1002/(SICI)1097-0290(19970905)55:5<715::CO;2-E)
- Cui, Y. Q., van der Lans, R., & Luyben, K. (1998). Effects of dissolved oxygen tension and mechanical forces on fungal morphology in submerged fermentation. *Biotechnology and Bioengineering*, 57(4), 409–419. [https://doi.org/10.1002/\(SICI\)1097-0290\(19980220\)57:4<409::CO;2-Q](https://doi.org/10.1002/(SICI)1097-0290(19980220)57:4<409::CO;2-Q)
- Epstein, N. (1989). On tortuosity and the tortuosity factor in flow and diffusion through porous media. *Chemical Engineering Science*, 44(3), 777–779. [https://doi.org/10.1016/0009-2509\(89\)85053-5](https://doi.org/10.1016/0009-2509(89)85053-5)
- Ericson, C. (2010). *Morgan Kaufmann series in interactive 3D technology. Real-time collision detection* (pp. 125–233). Elsevier.
- Fiedler, M. R. M., Barthel, L., Kubisch, C., Nai, C., & Meyer, V. (2018). Construction of an improved *Aspergillus niger* platform for enhanced glucoamylase secretion. *Microbial Cell Factories*, 17(1), 1–12. <https://doi.org/10.1186/s12934-018-0941-8>
- Fontaine, T., Beauvais, A., Loussert, C., Thevenard, B., Fulgsang, C. C., Ohno, N., Clavaud, C., Prevost, M. C., & Latgé, J. P. (2010). Cell wall alpha1-3glucans induce the aggregation of germinating conidia of *Aspergillus fumigatus*. *Fungal Genetics and Biology*, 47(8), 707–712. <https://doi.org/10.1016/j.fgb.2010.04.006>
- Glover, P. W. J., Gómez, J. B., Meredith, P. G., Hayashi, K., Sammonds, P. R., & Murrell, S. A. F. (1997). Damage of saturated rocks undergoing triaxial deformation using complex electrical conductivity measurements: Experimental results. *Physics and Chemistry of the Earth*, 22(1–2), 57–61. [https://doi.org/10.1016/S0079-1946\(97\)00078-5](https://doi.org/10.1016/S0079-1946(97)00078-5)
- He, X., Guo, Y., Li, M., Pan, N., & Wang, M. (2017). Effective gas diffusion coefficient in fibrous materials by mesoscopic modeling. *International Journal of Heat and Mass Transfer*, 107, 736–746. <https://doi.org/10.1016/j.ijheatmasstransfer.2016.11.097>
- Hille, A., Neu, T. R., Hempel, D. C., & Horn, H. (2005). Oxygen profiles and biomass distribution in biopellets of *Aspergillus niger*. *Biotechnology and Bioengineering*, 92(5), 614–623. <https://doi.org/10.1002/bit.20628>
- Hille, A., Neu, T. R., Hempel, D. C., & Horn, H. (2009). Effective diffusivities and mass fluxes in fungal biopellets. *Biotechnology and Bioengineering*, 103(6), 1202–1213. <https://doi.org/10.1002/bit.22351>
- Jung, S. M., Preston, D. J., Jung, H. Y., Deng, Z., Wang, E. N., & Kong, J. (2016). Porous Cu nanowire aerosplices from one-step assembly and their applications in heat dissipation. *Advanced Materials*, 28(7), 1413–1419. <https://doi.org/10.1002/adma.201504774>
- Ke, X., Prahl, J. M., Alexander, J. I. D., Wainright, J. S., Zawodzinski, T. A., & Savinell, R. F. (2018). Rechargeable redox flow batteries: Flow fields, stacks and design considerations. *Chemical Society Reviews*, 47(23), 8721–8743. <https://doi.org/10.1039/c8cs00072g>
- Keller, N. P. (2019). Fungal secondary metabolism: Regulation, function and drug discovery. *Nature Reviews Microbiology*, 17(3), 167–180. <https://doi.org/10.1038/s41579-018-0121-1>
- Kim, M. J., Seo, Y., Cruz, M. A., & Wiley, B. J. (2019). Metal nanowire felt as a flow-through electrode for high-productivity electrochemistry. *ACS Nano*, 13(6), 6998–7009. <https://doi.org/10.1021/acsnano.9b02058>
- Kozeny, J. (1927). Über kapillare Leitung des Wassers im Boden. *Royal Academy of Science, Vienna*, 136, 271–306.
- Kwon, M. J., Arentshorst, M., Roos, E. D., van den Hondel, C. A. M. J. J., Meyer, V., & Ram, A. F. J. (2011). Functional characterization of Rho GTPases in *Aspergillus niger* uncovers conserved and diverged roles of Rho proteins within filamentous fungi. *Molecular Microbiology*, 79(5), 1151–1167. <https://doi.org/10.1111/j.1365-2958.2010.07524.x>
- Lehmann, A., Zheng, W., Soutschek, K., Roy, J., Yurkov, A. M., & Rillig, M. C. (2019). Tradeoffs in hyphal traits determine mycelium architecture in saprobic fungi. *Scientific Reports*, 9(1), 14152. <https://doi.org/10.1038/s41598-019-50565-7>
- Lejeune, R., & Baron, G. V. (1997). Simulation of growth of a filamentous fungus in 3 dimensions. *Biotechnology and Bioengineering*, 53(2), 139–150. [https://doi.org/10.1002/\(SICI\)1097-0290\(19970120\)53:2<139::CO;2-P](https://doi.org/10.1002/(SICI)1097-0290(19970120)53:2<139::CO;2-P)
- McLachlan, G. J., & Peel, D. (2000). Finite mixture models. Wiley series in probability and statistics Applied probability and statistics section. Wiley.
- Metz, B., & Kossen, N.W.F. (1977). The growth of molds in the form of pellets—a literature review. *Biotechnology and Bioengineering*, 19(6), 781–799. <https://doi.org/10.1002/bit.260190602>
- Meyer, F. (1994). Topographic distance and watershed lines. *Signal Processing*, 38(1), 113–125. [https://doi.org/10.1016/0165-1684\(94\)90060-4](https://doi.org/10.1016/0165-1684(94)90060-4)
- Meyer, V., Basenko, E. Y., Benz, J. P., Braus, G. H., Caddick, M. X., Csukai, M., de Vries, R. P., Endy, D., Frisvad, J. C., Gunde-Cimerman, N., Haarmann, T., Hadar, Y., Hansen, K., Johnson, R. I., Keller, N. P., Kraševc, N., Mortensen, U. H., Perez, R., Ram, A. F. J., ... Wösten, H. A. B. (2020). Growing a circular economy with fungal biotechnology: A white paper. *Fungal Biology and Biotechnology*, 7(1), 5. <https://doi.org/10.1186/s40694-020-00095-z>
- Meyerhoff, J., Tiller, V., & Bellgardt, K.-H. (1995). Two mathematical models for the development of a single microbial pellet. *Bioprocess Engineering*, 12(6), 305–313. <https://doi.org/10.1007/BF00369507>
- Nepal, K. K., & Wang, G. (2019). Streptomyces: Surrogate hosts for the genetic manipulation of biosynthetic gene clusters and production of natural products. *Biotechnology Advances*, 37(1), 1–20. <https://doi.org/10.1016/j.biotechadv.2018.10.003>
- Nielsen, J. (1996). Modelling the morphology of filamentous microorganisms. *Trends in Biotechnology*, 14(11), 438–443. [https://doi.org/10.1016/0167-7799\(96\)10055-X](https://doi.org/10.1016/0167-7799(96)10055-X)
- Nielsen, J. C., Grijseels, S., Prigent, S., Ji, B., Dainat, J., Nielsen, K. F., Frisvad, J. C., Workman, M., & Nielsen, J. (2017). Global analysis of biosynthetic gene clusters reveals vast potential of secondary metabolite production in *Penicillium* species. *Nature Microbiology*, 2, 17044. <https://doi.org/10.1038/nmicrobiol.2017.44>
- Otsu, N. (1979). A threshold selection method from gray-level histograms. *Systems, Man and Cybernetics, IEEE Transactions on*, 9(1), 62–66. <https://doi.org/10.1109/TSMC.1979.4310076>
- Panerai, F., Ferguson, J. C., Lachaud, J., Martin, A., Gasch, M. J., & Mansour, N. N. (2017). Micro-tomography based analysis of thermal conductivity, diffusivity and oxidation behavior of rigid and flexible fibrous insulators. *International Journal of Heat and Mass Transfer*, 108, 801–811. <https://doi.org/10.1016/j.ijheatmasstransfer.2016.12.048>

- Papagianni, M. (2004). Fungal morphology and metabolite production in submerged mycelial processes. *Biotechnology Advances*, 22(3), 189–259. <https://doi.org/10.1016/j.biotechadv.2003.09.005>
- Schmideder, S., Barthel, L., Friedrich, T., Thalhammer, M., Kovačević, T., Niessen, L., Meyer, V., & Briesen, H. (2019). An X-ray microtomography-based method for detailed analysis of the three-dimensional morphology of fungal pellets. *Biotechnology and Bioengineering*, 116(6), 1355–1365. <https://doi.org/10.1002/bit.26956>
- Schmideder, S., Barthel, L., Müller, H., Meyer, V., & Briesen, H. (2019). From three-dimensional morphology to effective diffusivity in filamentous fungal pellets. *Biotechnology and Bioengineering*, 116(12), 3360–3371. <https://doi.org/10.1002/bit.27166>
- Schrinner, K., Veiter, L., Schmideder, S., Doppler, P., Schrader, M., Münch, N., Althof, K., Kwade, A., Briesen, H., Herwig, C., & Krull, R. (2020). Morphological and physiological characterization of filamentous *Lentzea aerocolonigenes*: Comparison of biopellets by microscopy and flow cytometry. *PLoS One*, 15(6), e0234125. <https://doi.org/10.1371/journal.pone.0234125>
- Silin, D., & Patzek, T. (2006). Pore space morphology analysis using maximal inscribed spheres. *Physica A: Statistical Mechanics and Its Applications*, 371(2), 336–360. <https://doi.org/10.1016/j.physa.2006.04.048>
- Tamayol, A., McGregor, F., & Bahrami, M. (2012). Single phase through-plane permeability of carbon paper gas diffusion layers. *Journal of Power Sources*, 204, 94–99. <https://doi.org/10.1016/j.jpowsour.2011.11.084>
- Tang, X., & Yan, X. (2017). Acoustic energy absorption properties of fibrous materials: A review. *Composites, Part A: Applied Science and Manufacturing*, 101, 360–380. <https://doi.org/10.1016/j.compositesa.2017.07.002>
- Taylor, D. L., Hollingsworth, T. N., McFarland, J. W., Lennon, N. J., Nusbaum, C., & Ruess, R. W. (2014). A first comprehensive census of fungi in soil reveals both hyperdiversity and fine-scale niche partitioning. *Ecological Monographs*, 84(1), 3–20. <https://doi.org/10.1890/12-1693.1>
- Tegelaar, M., Aerts, D., Teertstra, W. R., & Wösten, H. A. B. (2020). Spatial induction of genes encoding secreted proteins in micro-colonies of *Aspergillus niger*. *Scientific Reports*, 10(1), 1536. <https://doi.org/10.1038/s41598-020-58535-0>
- Tomadakis, M. M., & Robertson, T. J. (2005). Viscous permeability of random fiber structures: Comparison of electrical and diffusional estimates with experimental and analytical results. *Journal of Composite Materials*, 39(2), 163–188. <https://doi.org/10.1177/0021998305046438>
- Tomadakis, M. M., & Sotirchos, S. V. (1991). Effects of fiber orientation and overlapping on knudsen, transition, and ordinary regime diffusion in fibrous substrates. *MRS Proceedings*, 250, 221. <https://doi.org/10.1557/PROC-250-221>
- Tomadakis, M. M., & Sotirchos, S. V. (1993). Effective diffusivities and conductivities of random dispersions of nonoverlapping and partially overlapping unidirectional fibers. *The Journal of Chemical Physics*, 99(12), 9820–9827. <https://doi.org/10.1063/1.465464>
- Tomadakis, M. M., & Sotirchos, S. V. (1993). Ordinary and transition regime diffusion in random fiber structures. *AIChE Journal*, 39(3), 397–412. <https://doi.org/10.1002/aic.690390304>
- Tomadakis, M. M., & Sotirchos, S. V. (1993). Transport properties of random arrays of freely overlapping cylinders with various orientation distributions. *The Journal of Chemical Physics*, 98(1), 616–626. <https://doi.org/10.1063/1.464604>
- Veiter, L., & Herwig, C. (2019). The filamentous fungus *Penicillium chrysogenum* analysed via flow cytometry—a fast and statistically sound insight into morphology and viability. *Applied Microbiology and Biotechnology*, 103(16), 6725–6735. <https://doi.org/10.1007/s00253-019-09943-4>
- Veiter, L., Kubicek, M., Hutter, H., Pittenauer, E., Herwig, C., & Slouka, C. (2020). Study of metabolism and identification of productive regions in filamentous fungi via spatially resolved time-of-flight secondary ion mass spectrometry. *Analytical and Bioanalytical Chemistry*, 412(9), 2081–2088. <https://doi.org/10.1007/s00216-019-01980-2>
- Veiter, L., Rajamanickam, V., & Herwig, C. (2018). The filamentous fungal pellet-relationship between morphology and productivity. *Applied Microbiology and Biotechnology*, 102(7), 2997–3006. <https://doi.org/10.1007/s00253-018-8818-7>
- Velichko, A., Wiegmann, A., & Mücklich, F. (2009). Estimation of the effective conductivities of complex cast iron microstructures using FIB-tomographic analysis. *Acta Materialia*, 57(17), 5023–5035. <https://doi.org/10.1016/j.actamat.2009.07.004>
- Wang, Q., Zhong, C., & Xiao, H. (2020). Genetic engineering of filamentous fungi for efficient protein expression and secretion. *Frontiers in Bioengineering and Biotechnology*, 8, 293. <https://doi.org/10.3389/fbioe.2020.00293>
- Ward, O.P. (2012). Production of recombinant proteins by filamentous fungi. *Biotechnology Advances*, 30(5), 1119–1139. <https://doi.org/10.1016/j.biotechadv.2011.09.012>
- Wiegmann, A., & Zemitis, A. (2006). EJ-HEAT: A fast explicit jump harmonic averaging solver for the effective heat conductivity of composite materials (Fraunhofer ITWM Report, 94).
- Witten, T. A., & Sander, L. M. (1983). Diffusion-limited aggregation. *Physical Review B*, 27(9), 5686–5697. <https://doi.org/10.1103/PhysRevB.27.5686>
- Wittier, R., Baumgartl, H., Lübbers, D. W., & Schügerl, K. (1986). Investigations of oxygen transfer into *Penicillium chrysogenum* pellets by microprobe measurements. *Biotechnology and Bioengineering*, 28(7), 1024–1036. <https://doi.org/10.1002/bit.260280713>
- Wösten, H. A. B. (2019). Filamentous fungi for the production of enzymes, chemicals and materials. *Current Opinion in Biotechnology*, 59, 65–70. <https://doi.org/10.1016/j.copbio.2019.02.010>
- Yang, H., Reichl, U., King, R., & Gilles, E. D. (1992). Measurement and simulation of the morphological development of filamentous microorganisms. *Biotechnology and Bioengineering*, 39(1), 44–48. <https://doi.org/10.1002/bit.260390108>
- Yaws, C. L. (2009). *Transport properties of chemicals and hydrocarbons* (pp. 502–596). Andrew.
- Yuan, J., Liu, X., Akbulut, O., Hu, J., Suib, S. L., Kong, J., & Stellacci, F. (2008). Superwetting nanowire membranes for selective absorption. *Nature Nanotechnology*, 3(6), 332–336. <https://doi.org/10.1038/nnano.2008.136>
- Zacchetti, B., Wösten, H. A. B., & Claessen, D. (2018). Multiscale heterogeneity in filamentous microbes. *Biotechnology Advances*, 36(8), 2138–2149. <https://doi.org/10.1016/j.biotechadv.2018.10.002>
- Zhang, J., & Zhang, J. (2016). The filamentous fungal pellet and forces driving its formation. *Critical Reviews in Biotechnology*, 36(6), 1066–1077. <https://doi.org/10.3109/07388551.2015.1084262>

## SUPPORTING INFORMATION

Additional supporting information may be found online in the Supporting Information section.

**How to cite this article:** Schmideder S, Müller H, Barthel L, et al. Universal law for diffusive mass transport through mycelial networks. *Biotechnology and Bioengineering*. 2021; 118:930–943. <https://doi.org/10.1002/bit.27622>